

State of Health Estimation for Lithium-ion batteries Based on Extreme Learning Machine with Improved Blinex Loss

Wentao Ma^{1,2,*}, Panfei Cai¹, Fengyuan Sun², Xiaofei Wang³, Junyu Gong⁴

¹ School of Electrical Engineering, Xi'an University of Technology, Xi'an 710048, China

² Guangxi Wireless Broadband Communication and Signal Processing Key Laboratory, Guilin University of Electronic Technology, Guilin 541004, China

³ School of Microelectronics, Xi'an Jiaotong University, Xi'an 710049, China

⁴ Xi'an Aerospace Minxin Technology Co., Ltd., Xi'an 710076, China

*E-mail: mawt@xaut.edu.cn

Received: 13 August 2022 / Accepted: 22 September 2022 / Published: 20 October 2022

The state of health (SOH) estimation for Lithium-ion batteries (LIBs) plays an important role in battery management system (BMS), and the data-driven based SOH estimate methods mainly depend on the measurement data which is usually corrupted by non-Gaussian noise or other random disturbances because BMS usually works under complex environmental conditions. To achieve more accurate and robust SOH estimation, a novel robust extreme learning machine (ELM) based SOH estimation method is proposed. An improved Blinex Loss (IB-Loss) function is defined to replace the mean square error (MSE) loss in traditional ELM, and a novel robust estimation method called ELM with IB-Loss (IB-ELM) is derived, which can reduce the effect of noise. Through the comprehensive analysis of the aging experimental data of LIBs, we extract health features (HFs) from the charging data as the input of the estimation model, and the gray relational analysis (GRA) is utilized to evaluate the correlation between HFs and SOH to determine the rationality of selected HFs. Finally, the battery datasets provided by NASA are used as the training set and testing set to verify the effectiveness of the proposed method, and experimental results show that it has higher estimation accuracy than other existing data-driven methods under non-Gaussian noise conditions.

Keywords: State of health estimation; Extreme learning machine; Improved Blinex Loss; Non-Gaussian noise

1. INTRODUCTION

The emergence of new energy electric vehicles (EVs) has just been changing the existing energy consumption mode dominated by oil, greatly reducing the utilization of non-renewable energy and the release of various exhaust pollutants, and playing a crucial role in building a green and clean environment.

LIBs have become the best choice for new energy EVs and energy storage systems [1, 2] because of their high energy density, long service life, high power tolerance, high rated voltage, light weight, low self-discharge rate, no memory effect and environmental friendliness [3]. But the capacity of LIBs will gradually decline with the increasing of the charge-discharge cycle number, and its performance will deteriorate due to aging and operating environment [4], which seriously affects the driving safety of EVs and the safety of human life and property. Consequently, achieving accurate SOH estimation for LIBs is an essential part of the BMS. Accurate SOH estimation can not only make full use of the performance of LIBs, but also improve more safe and reliable protection for the battery, so as to greatly prolong the service life of the battery system [5, 6].

Recently, more and more methods have been developed to estimate the SOH of LIBs. Generally speaking, the existing SOH estimation methods can be roughly divided into three categories: direct measurement methods, model-driven (MD) methods and data-driven (DD) methods. Direct measurement methods obtain the capacity or impedance of LIBs by specific experimental manipulations as well as calculations. The most common methods are open circuit voltage (OCV) method [7, 8] and coulomb counting method [9]. These methods are simple, convenient, easy to implement and with low computational complexity. However, the OCV method demands the battery to stand for a long time to achieve stable SOH estimation and Coulomb counting method can obtain the SOH of the battery only under the complete charge-discharge process. Therefore, these methods are not only time-consuming and labor-intensive, but also easily affected by the accuracy of voltage and current acquisition, making it difficult to achieve online estimation. In addition, measuring the battery impedance to estimate the current SOH of the battery is one of the methods currently used, which has high accuracy but easily affected by ambient temperature and measuring equipment.

To solve the problems brought by direct measurement methods, the MD methods are proposed. The MD methods simulate the aging phenomenon of LIBs by combining measurement data (voltage, current, and temperature) with electrochemical models (EMs) [10] or equivalent circuit models (ECMs), and estimate the battery's SOH directly or indirectly. The EMs comprehensively analyze the internal mechanism and chemical reaction of LIBs, establish the related mathematical equation, and construct the aging model from the essence of LIBs. Although the EMs can analyze the aging process of LIBs from the chemical reactions level, which have clear physical significance and high prediction accuracy, the construction of the EMs must clarify the complex chemical reactions inside LIBs, so more physical parameters inside LIBs need to be measured, which will lead to high computational complexity and great difficulty in practical application. The ECMs use the existing knowledge of circuit theory to fully simulate the operating characteristics of the battery with relatively small amount of calculation and high model accuracy, which are the most widely used battery model at present. Common ECMs include Rint model, Thevenin model, first-order RC model and second-order RC model [11], etc., which are often combined with various filters, such as Kalman filter (KF) [12-16], particle filter (PF) [17-20], H_∞ filter [21], or observers [22, 23] to estimate SOH. Although the above methods can achieve accurate estimation, there are still many shortcomings that their performance is highly dependent on the stability and accuracy of the developed battery model or observer, and the accurate battery model will seriously increase the computational complexity [24].

With the emergence of cloud devices and the development of artificial intelligence technology,

machine learning algorithms have made great progress in the field of power battery SOH estimation, forming DD battery SOH estimation methods. DD methods have received increasing attention from academia and industry due to the advantages of not involving complex physical models, flexibility, and model-free nature. This method completely relies on battery data, only analyzes and considers the factors affecting aging of LIBs from the data to establish estimation model, and achieves accurate SOH estimation with the least possible human intervention. DD model building greatly depends on the selected HFs, and suitable HFs are a prerequisite for accurate SOH estimation of LIBs which are usually extracted from online measurement data. Reference [25] proposed a new method for SOH estimation based on the combination of multiscale logistic regression (LR) and Gaussian process regression (GPR) which can not only track the degradation behavior of LIBs as they change, but also reduce the effects of local regeneration phenomena. Xiong *et al.* [26] improved the standard support vector machine (SVM) through weighting function and linear equation, and obtained an online SOH estimation method based on weighted least squares SVM (WLS-SVM), which improved the accuracy and robustness of the model. To address the problem of low accuracy of traditional estimation methods, Li *et al.* [27] achieved more accurate and robust SOH estimation by using an improved ant lion optimization algorithm to optimize the support vector regression (SVR) model. Except the methods mentioned above, many DD methods have also been used to achieve accurate SOH estimation, such as random forest regression (RFR) [28], radial basis function neural network (RBFNN) [29], relevance vector machine (RVM) [30], long short-term memory network (LSTM) [31] and so on. Although these methods can achieve good SOH estimation, the large amount of training data and their own complex model structure are unavoidable, which will undoubtedly make the training time longer, computationally more intensive, and require iterative adjustment, eventually leading to a decrease in the speed and accuracy of estimation. Moreover, achieving stable and accurate estimation is also an essential goal in the operation of EVs. To solve the above problems, Huang *et al.* [32] proposed a novel neural network method-ELM with faster learning speed, stronger generalization ability and higher computational efficiency which has been widely used in regression and prediction problems [33, 34]. Taking advantage of ELM, Guo *et al.* [35] proposed an ELM model with an ensemble learning structure for SOH estimation to reduce the estimation error of a single ELM model. Chen *et al.* [36] developed SOH estimation model for batteries based on a metabolic ELM which achieves SOH estimation for different types of batteries by building a degradation state model and adding error compensation. Li *et al.* [37] used the heuristic Kalman filter (HKF) algorithm to optimize the ELM and obtained an optimized estimation model HKF-ELM. Compared to existing models, faster and more accurate SOH estimation is achieved. In addition, considering the problem that the external information (voltage, current and temperature, etc.) of the battery is unstable and easy to fluctuate, Fu *et al.* [38] chose impedance as the HFs reflecting the aging state of the battery from the perspective of electrochemical impedance spectrum (EIS), and then realized the fast acquisition of EIS by improved fast Fourier transform (FFT), and finally realized the SOH estimation for LIBs based on the regularized ELM. In a word, DD methods have many obvious advantages, especially ELM, which has been rapidly developed in the field of SOH estimation with its excellent performance.

However, the BMS often works in complex environmental conditions, which makes the measurement data used for model training vulnerable to non-Gaussian noise or other random disturbances. In this case, the DD methods with MSE may not be robust to SOH estimation, because

MSE is optimal when the data obey Gaussian distribution. Hence, the traditional ELM based on MSE is not suitable for SOH estimation in complex environment. How to design robust DD model becomes an urgent task for SOH estimation. Recently, a simple and robust Blinex loss (B-Loss) function is defined in [39] to design robust methods for credit risk evaluation. In this work, the square of error is used to replace the error in the definition of the original B-Loss, and then an IB-Loss is defined, which can be used as a novel robust cost for machine methods. Combining the outstanding performance of the ELM and B-Loss, we incorporate the IB-Loss into the ELM framework to study a new robust estimation model, called IB-ELM model and the proposed model is used to estimate SOH to address the problem of non-Gaussian noise disturbance in the measurement data used for training. The main contributions of this paper are as follows:

(1) Based on the B-Loss function, an IB-Loss function is defined, which can be used as a new robust learning criterion for neural network models due to its wide performance surface.

(2) Combining the traditional ELM with IB-Loss, a new robust ELM model is obtained, which greatly improves the robustness and estimation accuracy of the traditional ELM.

(3) Based on the NASA battery datasets, HFs are extracted from the charging data as the input of the model, and then GRA is used to evaluate the correlation between HFs and SOH to determine the rationality of the selected HFs. Next, IB-ELM model is used to estimate SOH under the interference of non-Gaussian noise. Through cross-experimental verification, this approach not only achieves robust SOH estimation, but also has high estimation accuracy.

The other work of this paper is organized as follows. Section 2 introduces the ELM model and defines the IB-Loss. Section 3 deduces the IB-ELM model and introduces the process of SOH estimation. Section 4, the performance of the proposed model is verified by experimental simulation. Section 5 summarizes the full text.

2. RELATED WORK

2.1. Extreme learning machine

As a single hidden layer feed-forward neural network (SLFNN) model, the ELM with random hidden layer nodes can obtain the only optimal solution after one calculation, i.e., there is no need for iterative adjustment. Therefore, it can perform with high learning efficiency, fast computing speed and strong generalization ability. The topology of ELM is shown in Fig.1, in which three layers are included (input layer, hidden layer and output layer). The neurons of each layer are fully connected.

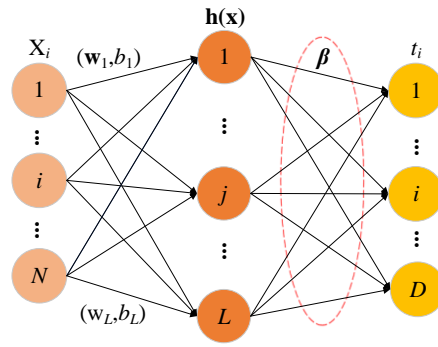


Figure 1. The topology of ELM.

Here setting the training samples as $\{\mathbf{x}_i, t_i\}_{i=1}^N$, where $\mathbf{x}_i = [x_{i1}, x_{i2}, \dots, x_{iN}]^T \in \mathbb{R}^N$ is the input vector and $t_i \in \mathbb{R}^D$ is target response. Then the output of the SLFNN with L hidden nodes can be defined as

$$y_i = \sum_{j=1}^L \beta_j g(\mathbf{w}_j \cdot \mathbf{x}_i + b_j) \tag{1}$$

where $g(\cdot)$ represents the activation function which usually is sigmoid function, $\mathbf{w}_j = [w_{j1}, w_{j2}, \dots, w_{jN}] \in \mathbb{R}^N$ and $b_j \in \mathbb{R}$ ($j = 1, 2, \dots, L$) are the input weight and bias of the j th hidden node, and $\beta_j \in \mathbb{R}$ denotes the weight of the link connecting the j th hidden node to the output node. Then the matrix form of the equation (1) can be expressed as

$$\mathbf{Y} = \mathbf{H}\boldsymbol{\beta} \tag{2}$$

where $\mathbf{Y} = (y_1, y_2, \dots, y_N)^T$, $\boldsymbol{\beta} = (\beta_1, \beta_2, \dots, \beta_N)^T$ and

$$\mathbf{H} = \begin{pmatrix} f(\mathbf{w}_1 \cdot \mathbf{x}_1 + b_1), & \dots & f(\mathbf{w}_L \cdot \mathbf{x}_1 + b_L) \\ \vdots & \ddots & \vdots \\ f(\mathbf{w}_1 \cdot \mathbf{x}_N + b_1), & \dots & f(\mathbf{w}_L \cdot \mathbf{x}_N + b_L) \end{pmatrix} \tag{3}$$

stands for the output matrix of the hidden layer.

Usually, the output weight vector $\boldsymbol{\beta}$ can be obtained by minimizing MSE as

$$\min_{\boldsymbol{\beta}} \|\mathbf{H}\boldsymbol{\beta} - \mathbf{T}\|^2 \tag{4}$$

where $\|\cdot\|$ denotes the Fresenius norm and $\mathbf{T} = (t_1, t_2, \dots, t_N)^T$ is the target response vector. The optimal solution of equation (4) can be solved by gradient descent method as

$$\boldsymbol{\beta} = \mathbf{H}^\dagger \mathbf{T} \tag{5}$$

Where $\mathbf{H}^\dagger = (\mathbf{H}^T \mathbf{H})^{-1} \mathbf{H}^T$ is the Moore-Penrose generalized inverse which can be obtained by orthogonal projection method when $\mathbf{H}^T \mathbf{H}$ is nonsingular. In addition, another learning criterion of the ELM with a regularization parameter λ to prevent over-fitting can be expressed as

$$J_{\text{MSE}}(\boldsymbol{\beta}) = \sum_{i=1}^N e_i^2 + \lambda \|\boldsymbol{\beta}\|_2^2 = \|\mathbf{H}\boldsymbol{\beta} - \mathbf{T}\|_2^2 + \lambda \|\boldsymbol{\beta}\|_2^2 \tag{6}$$

where $e_i = t_i - y_i$ is the error between the i^{th} target response and the i^{th} actual output. The optimal solution of $\boldsymbol{\beta}$ under the loss in (6) can be obtained by a pseudo inversion operation as

$$\boldsymbol{\beta} = [\mathbf{H}^T \mathbf{H} + \lambda \mathbf{I}]^{-1} \mathbf{H}^T \mathbf{T} \tag{7}$$

2.2. The improved Blinex loss

The traditional B-Loss is bounded and asymmetric, and it is robust to noise [39]. The expression is as follows:

$$L(e) = \frac{1}{\gamma} \left[1 - \frac{1}{1 + b(\exp(ae) - ae - 1)} \right] \tag{8}$$

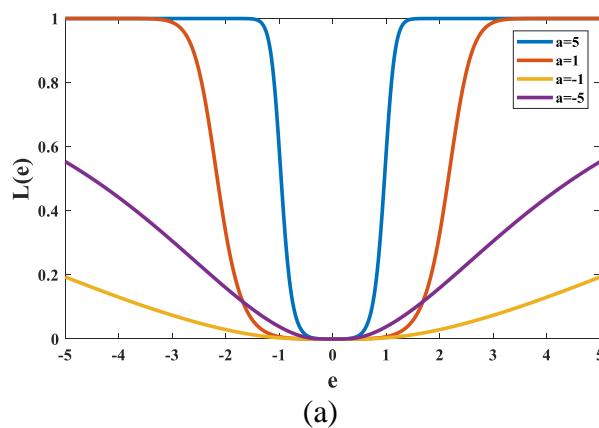
where $\exp(\cdot)$ represents exponential function, e is the error, a , b and γ are free parameters which control the performance shape of the proposed loss function.

However, it is hard to obtain an explicit solution when the B-Loss is used as the error criterion in ELM framework. To address this problem, we define an IB-Loss by using the square of error to replace the error in original B-Loss, which not only inherits the boundness of the traditional B-Loss, but also has symmetry, and can be solved very efficiently by using gradient optimization techniques. The IB-Loss is defined as (9)

$$L(e) = \frac{1}{\gamma} \left[1 - \frac{1}{1 + b(\exp(ae^2) - ae^2 - 1)} \right] \tag{9}$$

Fig.2 draws the IB-Loss image under distinct parameter combinations. From these figures, we can clearly see that each parameter has different effects on the performance of the function. Next, we will describe these three parameters in detail from several different angles.

The positive and negative of parameter a play a decisive role in the change trend of loss function. When $a > 0$, the IB-Loss function shows an exponential trend with the increase or decrease of e , while it changes almost linearly when $a < 0$. Therefore, the change trend of the IB-Loss function is affected by parameter a . For different changes of different problems, the corresponding parameter value a can be selected. In the IB-Loss function, ae^2 can be regarded as a whole. At this time, the change of a has an impact on the smoothness of the IB-Loss function. When a is positive, the larger value causes the steeper curve and the smaller value brings about the smoother curve when a is negative, as shown in Fig.2(a). As shown in Fig.2(b), parameter b reflects the steepness of the IB-Loss function. The larger b , the steeper the function curve. In addition, it can be clearly seen that the change degree of loss curve is much greater than that when $a > 0$. The parameter γ determines the peak range of the IB-Loss function which is set between 0 and $1/\gamma$. A larger parameter γ will lead to a smaller function peak, as shown in Fig.2(c). According to the above analysis, we know that the data by measure is easily contaminated by various noises [40], and the bounded IB-Loss helps to enhance the robustness.



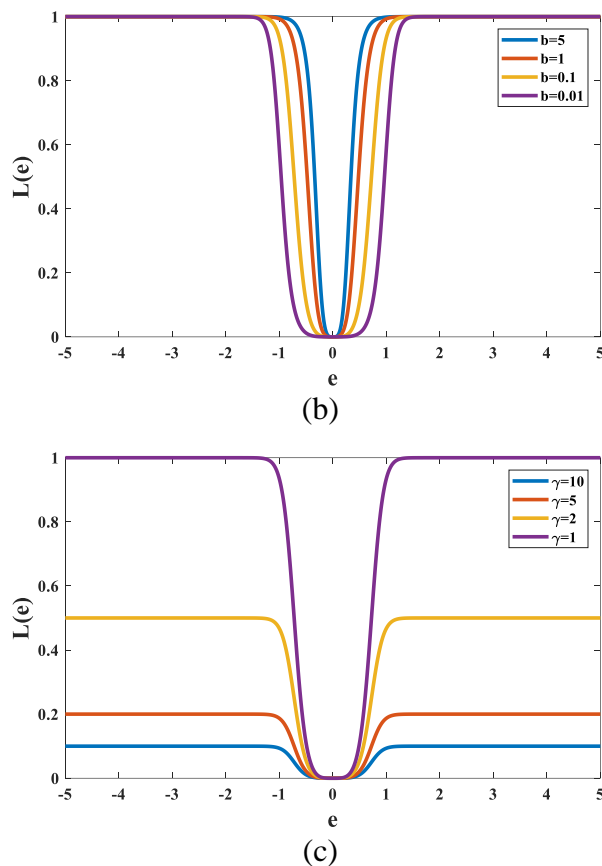


Figure 2. Improved Blinex loss function with different parameters a ($b = 0.01, \gamma = 1$), b ($a = 5, \gamma = 1$) and γ ($a = 5, b = 0.1$).

3. ELM WITH IB-LOSS FOR SOH ESTIMATION

3.1. ELM with IB-Loss

In this section, a novel robust ELM model with the IB-Loss is developed, we called it as IB-ELM model. In order to derive the novel ELM under the IB-Loss , a new error criterion with regularization term is further defined as

$$\begin{aligned}
 J_{IB-Loss}(\beta) &= J(\mathbf{T}, \mathbf{H}\beta) + \lambda \|\beta\|_2^2 \\
 &= \frac{1}{N} \sum_{i=1}^N \left[\frac{1}{\gamma} \left(1 - \frac{1}{1 + b(\exp(ae_i^2) - ae_i^2 - 1)} \right) \right] + \lambda \|\beta\|_2^2
 \end{aligned} \tag{10}$$

Note that unlike the MSE loss function in equation (6), the upper limit of the new loss function is 1.0, so it is not easy to be affected by large errors. Therefore, we use the gradient descent method to minimize loss function in equation (10) to find the optimal solution of the weight β . By solving the partial differential of the IB-Loss function with respect to the β and setting the result equal to zero, we can obtain the optimal solution form of the β as

$$\begin{aligned}
 & \frac{\partial J_{IB-Loss}(\boldsymbol{\beta})}{\partial \boldsymbol{\beta}} = 0 \\
 & \Rightarrow \frac{1}{\gamma N} \sum_{i=1}^N \frac{b[-2ae_i(\exp(ae_i^2))\mathbf{h}_i^T + 2ae_i\mathbf{h}_i^T]}{[1+b(\exp(ae_i^2) - ae_i^2 - 1)]^2} + 2\lambda\boldsymbol{\beta} = 0 \\
 & \Rightarrow \sum_{i=1}^N \frac{[1-\exp(ae_i^2)]e_i\mathbf{h}_i^T}{[1+b(\exp(ae_i^2) - ae_i^2 - 1)]^2} + \frac{\lambda\gamma N\boldsymbol{\beta}}{ab} = 0 \\
 & \Rightarrow \sum_{i=1}^N \frac{[1-\exp(ae_i^2)](t_i - \mathbf{h}_i\boldsymbol{\beta})\mathbf{h}_i^T}{[1+b(\exp(ae_i^2) - ae_i^2 - 1)]^2} + \lambda'\boldsymbol{\beta} = 0 \tag{11} \\
 & \Rightarrow \sum_{i=1}^N \frac{[1-\exp(ae_i^2)]t_i\mathbf{h}_i^T - [1-\exp(ae_i^2)]\mathbf{h}_i^T\mathbf{h}_i\boldsymbol{\beta}}{[1+b(\exp(ae_i^2) - ae_i^2 - 1)]^2} + \lambda'\boldsymbol{\beta} = 0 \\
 & \Rightarrow \sum_{i=1}^N f(e_i)t_i\mathbf{h}_i^T = \sum_{i=1}^N (f(e_i)\mathbf{h}_i^T\mathbf{h}_i\boldsymbol{\beta}) - \lambda'\boldsymbol{\beta} \\
 & \Rightarrow \boldsymbol{\beta} = [\mathbf{H}^T\boldsymbol{\Lambda}\mathbf{H} - \lambda'\mathbf{I}]^{-1}\mathbf{H}^T\boldsymbol{\Lambda}\mathbf{T}
 \end{aligned}$$

where $\lambda' = \lambda\gamma N / ab$ and $\boldsymbol{\Lambda}$ is a diagonal matrix with elements $\Lambda_{ii} = f(e_i)$, with

$$f(e_i) = (1 - \exp(ae_i^2)) / (1 + b(\exp(ae_i^2) - ae_i^2 - 1))^2 \tag{12}$$

It can be seen from equation (11) that the form of the optimal solution of $\boldsymbol{\beta}$ is not closed, and its value can be obtained only by solving the matrix $\boldsymbol{\Lambda}$ of the error term on the right side of the equation. So the equation (11) is a fixed-point equation in reality. Finally, this paper obtains the best result of weight in this way. The specific process of the algorithm is shown in Table 1.

Table 1. IB-ELM model.

Algorithm: IB-ELM
Input: samples $\{\mathbf{x}_i, t_i\}_{i=1}^N, \mathbf{x}_i \in \mathbb{R}^d, t_i \in \mathbb{R}$
Output: weight vector $\boldsymbol{\beta}$
Parameters setting : number of hidden nodes L , regularization parameter λ' , maximum number of iterations M , the parameters of loss function a, b, λ_1 and end condition \mathcal{E}
Initialization: Set $\boldsymbol{\beta}_0 = 0$ and randomly initialize the parameters w_j and b_j ($j = 1, 2, \dots, L$)
1: for $k=1, 2, \dots, M$ do
2: Calculation the error based on $\boldsymbol{\beta}_{k-1} : e_i = t_i - \mathbf{h}_i\boldsymbol{\beta}_{k-1}$
3: Calculation the diagonal matrix $\boldsymbol{\Lambda} : \Lambda_{ii} = f(e_i)$
4: Update the weight vector $\boldsymbol{\beta}_k : \boldsymbol{\beta}_k = [\mathbf{H}^T\boldsymbol{\Lambda}\mathbf{H} - \lambda'\mathbf{I}]^{-1}\mathbf{H}^T\boldsymbol{\Lambda}\mathbf{T}$
5: Until $ J_{IB}(\boldsymbol{\beta}_k) - J_{IB}(\boldsymbol{\beta}_{k-1}) < \mathcal{E}$
6: end for

3.2. SOH estimation using the IB-ELM

3.2.1. Definition of SOH

SOH as an evaluation index reflecting the current aging state of LIBs, has no definite standard at present. Common characterization methods include battery capacity, internal resistance and so on [41],

and the battery capacity is the most widely used characterization method. In this paper, we define the capacity as the current SOH of LIBs, as:

$$SOH = \frac{C_{current}}{C_{new}} \times 100\% \quad (13)$$

where C_{new} and $C_{current}$ denote the rated and current capacity, respectively. The SOH of newly manufactured LIBs is 100%. With the increasing use of LIBs, the aging state of batteries gradually intensifies, leading to the decline of SOH. When the capacity of the battery drops below 80% of the initial capacity, it is generally considered that it is no longer suitable for further use, and a new battery should be replaced for EVs immediately.

3.2.2. Data Analysis

In order to evaluate the performance and stability of the proposed model, the 18650 lithium battery public datasets with the rated capacity of 2Ah provided by NASA Ames Research Center [42] was selected as the data source of this article. In the following experiments, the B5, B6 and B7 battery datasets were used to extract HFs and SOH estimation. The accelerated aging test of LIBS was completed by continuously charging and discharging the battery at room temperature of 24°C. The specific process of charging was divided into constant current (CC) charging and constant voltage (CV) charging. First, the LIBs were charged with a constant current of 1.5A until the battery voltage reached the maximum cut-off voltage of 4.2V, and then continued to charge the battery with a constant voltage of 4.2V until the charging current dropped below 20mA. The discharge process was mainly to discharge the LIBs at a constant current of 2A until the battery voltage dropped below 2.7V, 2.5V and 2.2V respectively. The specific parameters related to NASA batteries are detailed in Table 2. The capacity change curves of NASA batteries are shown in Fig.3.

Table 2. Parameters of NASA Batteries

Properties	NASA Battery
Cathode material	LFP
Shape	Cylinder
Nominal capacity (mAh)	2000
Charge mode	CC/CV
Maximum cut-off voltage (V)	4.20
Minimum cut-off voltage (V)	2.7、2.5、2.2
End-of-charge current (mA)	20
Charging current (A)	1.5
Discharge current (A)	2

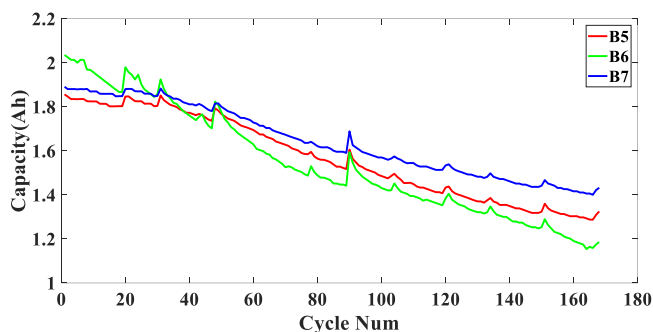
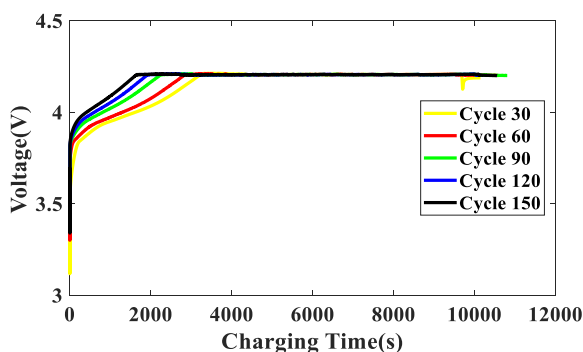


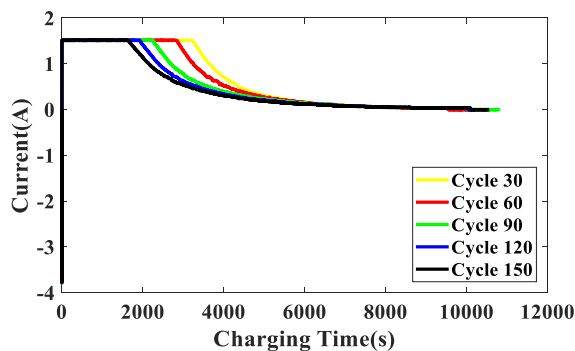
Figure 3. Capacity change curves of NASA batteries.

3.2.3. Feature Extraction

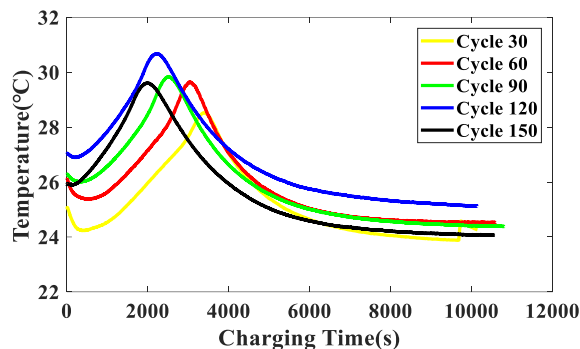
The HFs have a significant impact on understanding and estimating the current SOH of LIBs, and thus they need to be easy to obtain, simple to compute, and effective against interference. During the operation of EVs, the discharge mode of batteries is random and unpredictable [43] due to the complexity and uncertainty of the environment, so it is difficult to achieve accurate SOH estimation through discharge data. However, in most cases, the charging mode of LIBs is unified, and the energy is obtained from the power grid in a specific mode. Therefore, we choose relatively stable charging data and capacity change curves to extract HFs and realize SOH estimation.



(a) Voltage Curve



(b) Current Curve



(c) Temperature Curve

Figure 4. CC-CV charging profiles under different cycles.

In the accelerated aging experiment of LIBS, as the number of charge-discharge cycles gradually increases, we can clearly see from the charging curves that the charging time of the battery under the two modes has changed significantly. These changes are closely related to the aging of batteries, and reflect the changes of battery health status to a certain extent. Fig.4 shows the CC-CV charging curves of B5 battery under different cycles. As can be seen from Fig.4 (a), the charging duration in CV mode increases with the increase of the number of cycles. CV duration directly affects the charging capacity of the battery in CV mode, and also represents the polarization characteristics of the battery. As the number of cycles increases, the aging and polarization of the battery will gradually intensify, resulting in an increase in CV duration. In the actual operation of EVs, it is difficult to obtain the current remaining capacity and usage of batteries. Therefore, the relationship between CV duration and SOH is found by analyzing the charging voltage curves of LIBs, and the CV duration is extracted as a HF and expressed as F_1 , as shown in Fig.5.

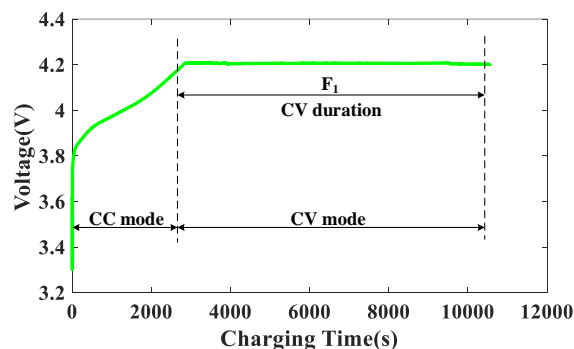


Figure 5. Selection of feature in charging voltage curve.

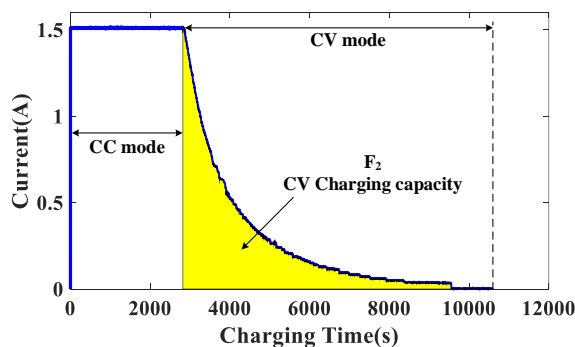


Figure 6. Selection of feature in charging current curve.

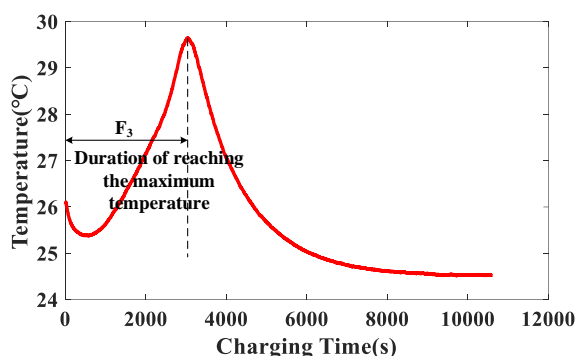


Figure 7. Selection of feature in charging temperature curve.

Fig.4(b) gives the charging current curves under different cycle times. We can see that the charging time in the CV stage increases significantly with the cycle experiment, which makes the charging capacity in the CV mode also tend to increase. In addition, there are also large fluctuations in the CV charging capacity around some cycle times. It can be seen that there is also a certain correlation between CV charging capacity and SOH. The CV charging capacity is extracted as another HF and denoted as F_2 , as shown in Fig.6.

When LIBs are charging, the variation curves of its shell temperature with the number of cycles is shown in Fig.4(c). As the increase of cycle times, the maximum temperature that LIBs can reach during the charging process shows a trend of first increasing and then decreasing, and the time to reach the maximum temperature point is gradually advanced. This is because the aging of LIBs brings about the continuous increase of internal resistance, so that the heat generated by the battery during CC process also increases, which in turn leads to a gradual increase in the maximum temperature of the battery. However, as the aging degree intensifies, the increase of the internal resistance of the battery gradually slows down, and CC duration is also significantly shortened, which eventually leads to a gradual decrease in the heat generated by the battery, and thus the maximum temperature that the battery can reach during charging will also decrease. To sum up, by analyzing the temperature change law of LIBs during charging, the duration of reaching the maximum temperature is selected as a HF, expressed as F_3 , and as shown in Fig.7. For further analysis and comparison, all obtained HFs were normalized.

3.2.4. Gray Relational Analysis for Extracted Features with SOH

In practice, the accuracy of the estimation model benefits from the selection of input vectors, which are affected by the actual application scenario and the correlation between HFs and estimated objects.

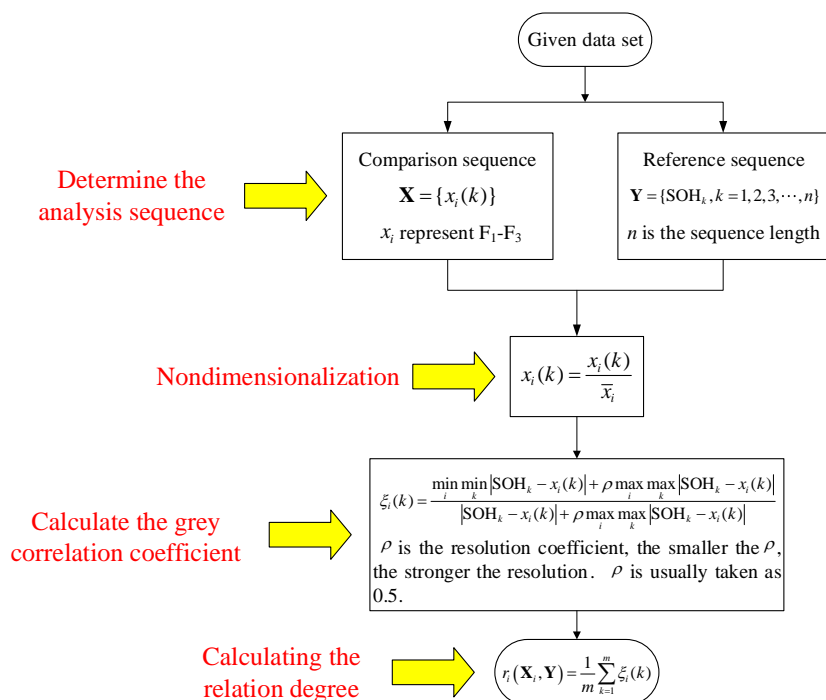


Figure 8. The specific implementation flow chart of GRA.

Therefore, appraising the correlation between SOH and HFs is a significant step to determine the input variables of the model. In order to determine the rationality of the selected HFs, GRA is used to evaluate the relationship between SOH and HFs [44] in this work. The principle of GRA is to measure the degree of correlation between factors according to the similarity or difference of development trends between factors. If the change trend of the two factors is consistent, the correlation degree between them is large, on the contrary, the correlation degree is small. The specific implementation flow chart of GRA is shown in Fig.8. Table 3 gives the GRA of three HFs and SOH. According to the evaluation rules of GRA, the closer the grey correlation degree r is to 1, the stronger the correlation is. GRA results show that the correlation between each HF and SOH is greater than 0.5, so the HFs selected in this paper are reasonable.

Table 3. GRA results between SOH and HFs.

	NASA battery		
	B5	B6	B7
F_1	0.5470	0.6191	0.5767
F_2	0.5499	0.5251	0.5975
F_3	0.8306	0.7539	0.6949

3.2.5. Evaluation Criteria

In order to evaluate the estimation performance of the proposed method, the maximum absolute error (MAE), MSE, root mean square error (RMSE) and symmetric mean absolute percentage error (SMAPE) are used as the criteria to evaluate the performance of the model. The aforementioned indexes can comprehensively evaluate the average estimation performance, of which smaller value implies better estimation accuracy, and they are defined as:

$$\left\{ \begin{array}{l} MAE = \max |y_i - \hat{y}_i| \\ MSE = \frac{1}{N} \sum_{i=1}^N (y_i - \hat{y}_i)^2 \\ RMSE = \sqrt{\frac{1}{N} \sum_{i=1}^N (y_i - \hat{y}_i)^2} \\ SMAPE = \frac{100\%}{2N} \sum_{i=1}^N \left| \frac{y_i - \hat{y}_i}{|y_i| + |\hat{y}_i|} \right| \end{array} \right. \quad (14)$$

where N is the total number of samples, y_i and \hat{y}_i are the measured value and estimated value of the i^{th} sample.

To sum up, the specific process of the network model for SOH estimation proposed in this paper is as follows:

Step 1: Data collection. The data (voltage, current and temperature) obtained from each charge discharge cycle will be used to select the HFs, and then form the input vector. The SOH determined after each charge discharge cycle can be used as the output of the model, which can be represented as $\{x_k, y_k\}_{k=1}^N$, and each sample can be written as $y_k = [\text{SOH}_k]$.

Step 2: Feature extraction. The voltage, current and temperature change curves are obtained from the charging data in **Step 1**, and then HFs related to SOH change are selected, denoted as $x_k = [F_1, F_2, F_3]$.

Step 3: Correlation analysis. The correlation between HFs and SOH is calculated by GRA to prove the rationality of the selected HFs.

Step 4: Formation of training and testing sets. The suitable training and testing sets are determined with the data of charge-discharge cycles under different capacity changes.

Step 5: Data preprocessing. The unified normalization of the extracted HFs can not only speed up the calculation speed of the model, but also increase the estimation accuracy of the model.

Step 6: Parameter setting. Selecting suitable static and dynamic parameters for IB-ELM to facilitate different data distribution problems.

Step 7: Model training. By using the training data to train the proposed IB-ELM model to obtain the optimal weight vector.

Step 8: Model testing. When the model training is completed, we input the test data into the trained network model to obtain the corresponding SOH estimation. Through the above-mentioned evaluation criteria (MSE, RMSE, MAE and SMAPE), we can distinctly understand the estimation performance of each model. Fig.9 shows the specific flow of IB-ELM for SOH estimation.

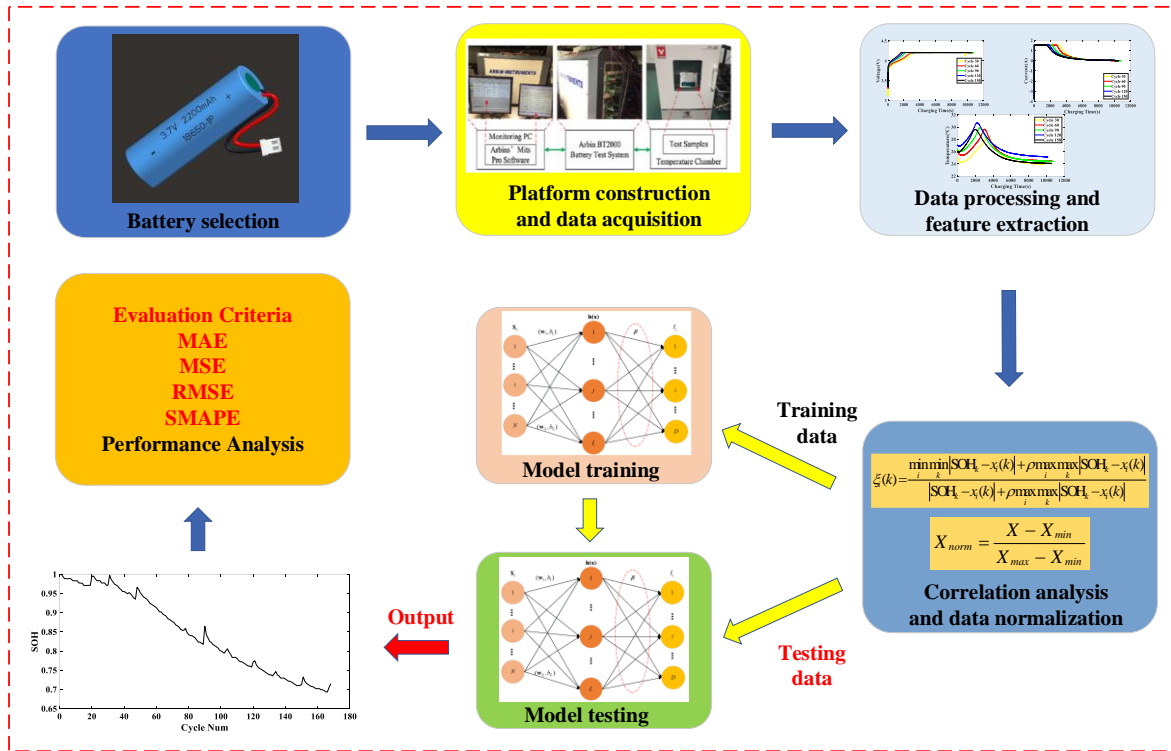


Figure 9. Flow chart of SOH estimation.

4. RESULTS AND DISCUSSION

Since BMS usually works under complex environmental conditions, the real SOH data are vulnerable to non-Gaussian noise or other random interference, which makes it difficult to obtain the actual data through the measurement method, which may eventually lead to measurement errors in the data used for model training. Thus, the noise interference in SOH data cannot be ignored. In this chapter, we carry out experimental simulation and compare it with conventional neural network methods to verify the function of the method studied in this paper under the interference of non-Gaussian noise.

The non-Gaussian noise $v(i)$ is a weighted combination of two noises in the form of $v(i) = (1 - a(i))A(i) + a(i)B(i)$, where $a(i)$ is a binary independent identically distributed process with probability mass $\Pr\{a(i) = 1\} = c, \Pr\{a(i) = 0\} = 1 - c (0 \leq c \leq 1)$. $A(i)$ is background noise and $B(i)$ is abnormal noise. $A(i)$ and $B(i)$ are independent of each other and both are independent of $a(i)$ with variances σ_A^2 and σ_B^2 . Generally, the variance of $B(i)$ is much larger than the variance of $A(i)$, so $B(i)$ can produce large outliers. In this section, c is set to 0.05. $B(i)$ is the zero-mean Gaussian noise with $\sigma_B^2 = 2.0$ and $A(i)$ is the mean noise uniformly distributed in $[0, 0.1]$. In addition, all experiments were completed under the interference of non-Gaussian noise $v(i)$.

Case 1 SOH estimation under B5 as the training set

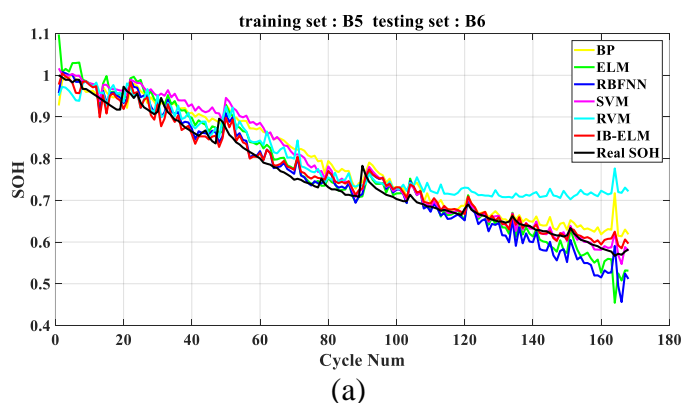
Based on the aging data of NASA battery datasets, the proposed method is experimentally verified and analyzed, and compared with the existing DD methods BP [45], ELM [38], RBFNN [29],

SVM [26] and RVM [30]. The parameters of all models and the experimental environment should be as consistent as possible. As shown in Table 4, B5, B6 and B7 are training set and testing set respectively to realize cross-validation. And the values of free parameters of IB-ELM model under different conditions are also given in Table 4. Moreover, considering the interference of non-Gaussian noise, the number of hidden layer neurons in BP, ELM, RBFNN and IB-ELM is 10. Finally, the average values of several independent Monte Carlo experiments are given to ensure the validity and reliability of the results.

Table 4. Free parameters settings of IB-ELM model and distribution of training and testing sets.

Training set	Testing set	free parameters
B5	B6	$a = 3, b = 2, \gamma = 1$
	B7	$a = 5, b = 10, \gamma = 1$
B6	B5	$a = 5, b = 10, \gamma = 1$
	B7	$a = 3, b = 2, \gamma = 1$
B7	B5	$a = 5, b = 10, \gamma = 1$
	B6	$a = 3, b = 2, \gamma = 1$

The HF_s of B5, B6, and B7 batteries are extracted as the input of the model, and their corresponding SOH_s are used as the output of the model, and then all models are trained and tested. First, we use B5 battery as the training set, B6 and B7 battery as the testing set respectively to verify the performance of the proposed model. Fig.10-11 show the SOH estimation results and absolute error curves for each model under non-Gaussian noise. Fig.12 presents the performance results of all models under different evaluation criteria. It can be clearly seen from Fig.10-11 that BP has great fluctuations in the estimation process, with low estimation accuracy and poor effect. This is because BP is a simple neural network, which is easily disturbed by noise and is very sensitive to noise. The traditional ELM and RBFNN based on MSE is optimal only under Gaussian noise, and thus its performance shows a large degradation in the case of non-Gaussian noise.



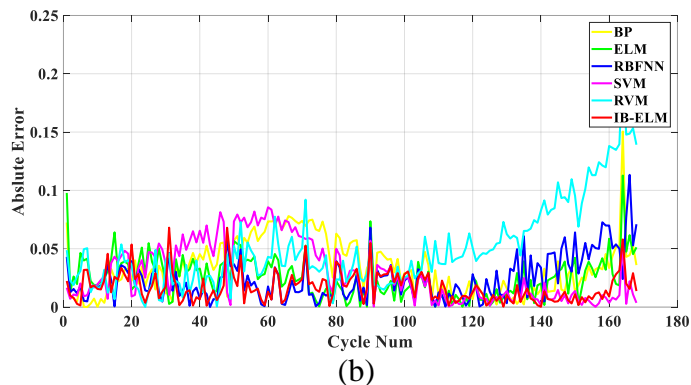


Figure 10. SOH estimation results and absolute error under different models for B6 with training set B5. (a) Estimation results. (b) Absolute Error.

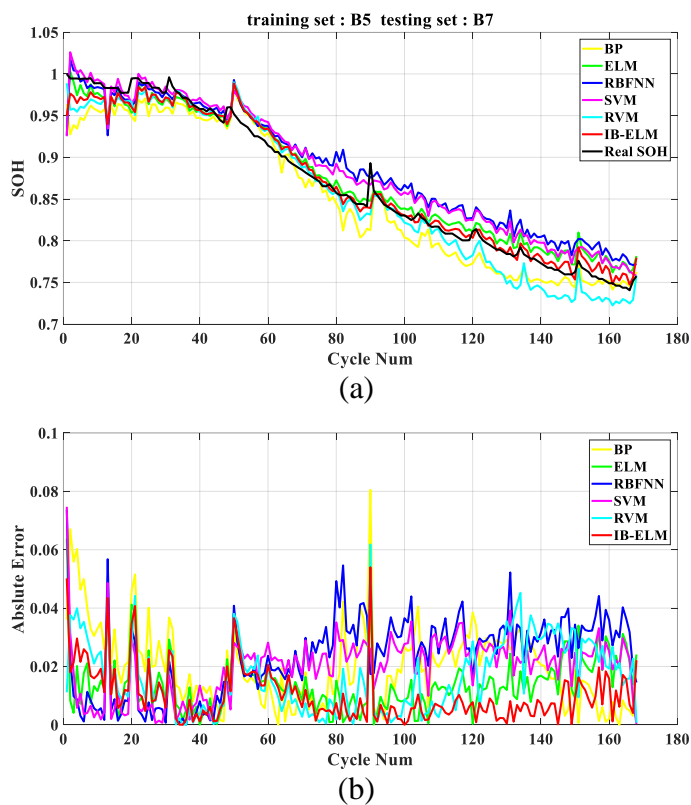


Figure 11. SOH estimation results and absolute error under different models for B7 with training set B5. (a) Estimation results. (b) Absolute Error.

At the same time, the estimation accuracy and performance of SVM and RVM also decrease under the interference of noise. Compared with the above methods, the model proposed in this paper still has good stability, robustness and lower estimation error under the interference of non-Gaussian noise due to its wider performance surface. For example, when B7 battery is used as the testing set, it can be seen from Fig.11 that the mean absolute error of the IB-ELM model is kept below 3%. As shown in Fig.12, compared with B6 battery as the testing set, the performance of all models is improved when

B7 battery is used as the testing set. In particular, the MSE, RMSE, MAE and MAPE of the model proposed in this paper reached 1.89×10^{-4} , 1.37%, 1.01% and 2.8×10^{-3} respectively. This is because the capacity change curves of B5 battery and B7 battery have the same change trend, and the corresponding HF's also have similar change characteristics, leading to the improvement of the estimation accuracy of the model.

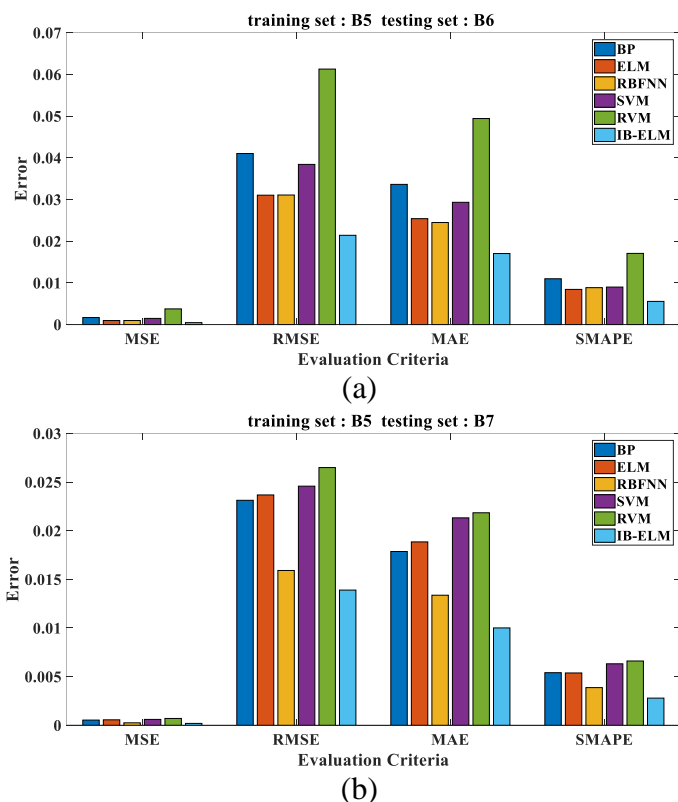


Figure 12. Results of performance evaluation criteria for different models with different testing sets. (a)B6. (b)B7.

Case 2 SOH estimation under B6 as the training set

Then we take B6 battery as the training set, B5 and B7 battery as the testing set respectively to verify the performance of the proposed model. The SOH estimation results and absolute error curves of each model under non-Gaussian noise are given in Fig.13-14. The performance results of all models under different evaluation criteria are given in Fig.15. It can be seen that the estimation accuracy and performance of all models are greatly reduced when the B6 battery is used as the training set. This is because the capacity change curve of B6 battery fluctuates greatly compared with B5 and B7. Although there are similarities between them, there are still great differences in general. Due to different working environments and manufacturing methods, even the same batch or same type of battery will have a very different aging process. As a result, all models show large estimation biases under the dual influence of non-Gaussian noise and the dataset. Although there are inevitable deviations in the model proposed in this paper, it is still within the acceptable range. The mean absolute errors are kept at about 4%.

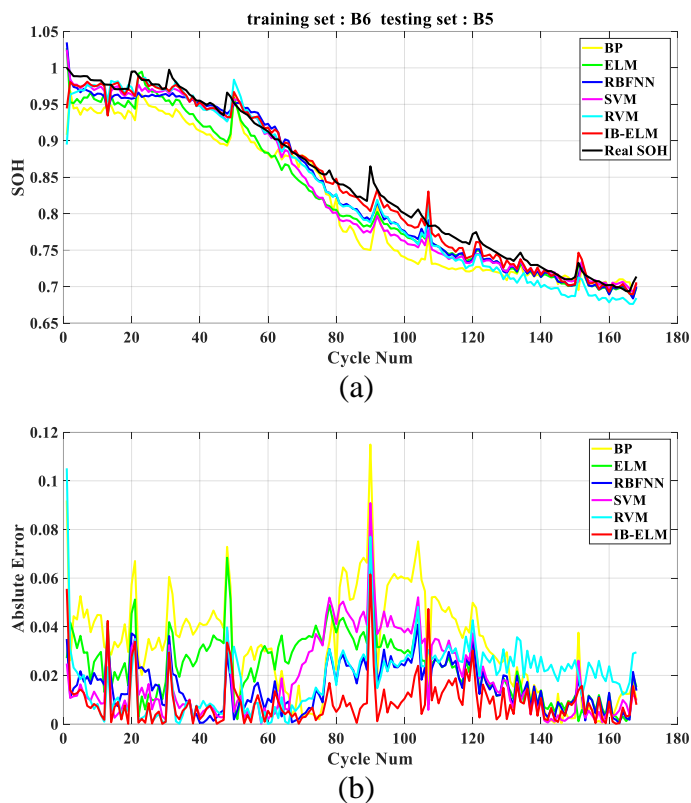


Figure 13. SOH estimation results and absolute error under different models for B5 with training set B6. (a) Estimation results. (b) Absolute Error.

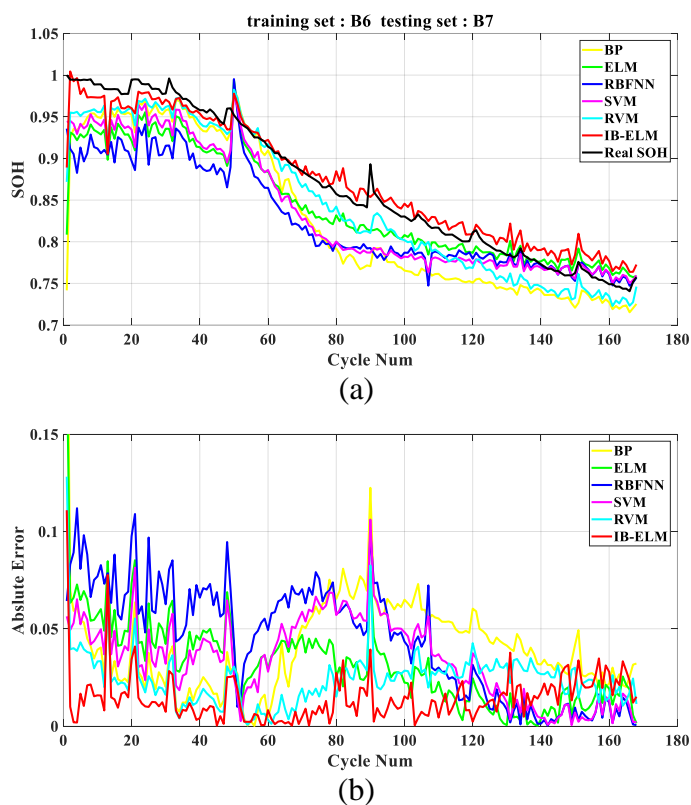


Figure 14. SOH estimation results and absolute error under different models for B7 with training set B6. (a) Estimation results. (b) Absolute Error.

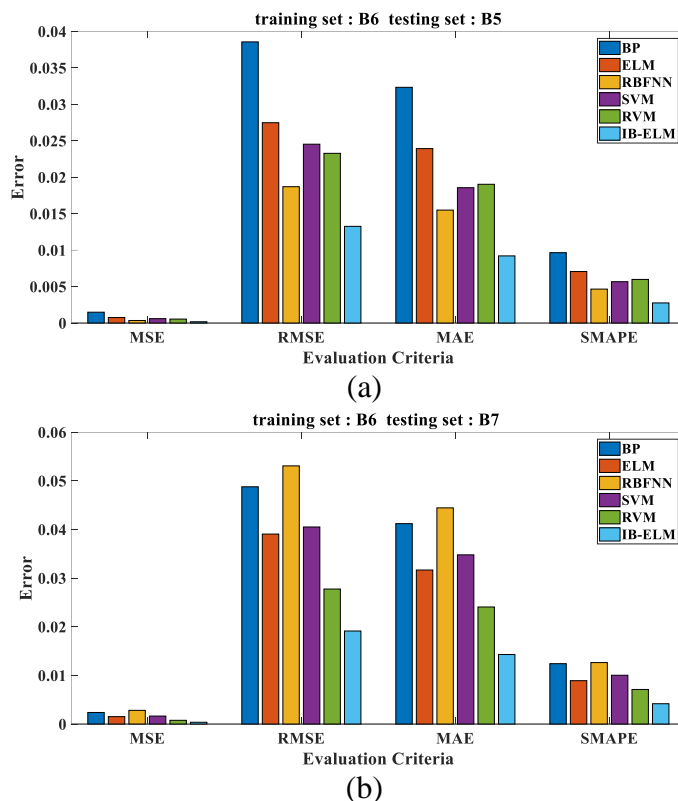


Figure 15. Results of performance evaluation criteria for different models with different testing sets. (a)B5. (b)B7.

As shown in Fig.15, when the training set is B6 battery and the testing set is B7 battery, the corresponding MSE, RMSE, MAE and MAPE of IB-ELM are 3.66×10^{-4} , 1.91%, 1.43% and 4.2×10^{-3} respectively. Thus it can be seen that the model proposed in this paper can achieve better estimation even under complex conditions.

Case 3 SOH estimation under B7 as the training set

Finally, we use B7 battery as the training set, B5 and B6 battery as the testing set to verify the performance of the proposed model. Fig.16-17 show the SOH estimation results and absolute error curves for each model under non-Gaussian noise. Fig.18 presents the performance results of all models under different evaluation criteria. As you can see, the estimated effect is similar to that of **Case 1**. Here we will not go into too much detail. In this case, the model proposed in this paper also has accurate estimation accuracy and stability compared to the existing DD methods (BP, ELM, RBFNN, SVM and RVM). As can be seen from Fig.16-17, the mean absolute error mostly stays within 5%, especially when the testing set is B5 battery, the mean absolute error is kept around 3%. As shown in Fig.18, since B5 and B7 battery have similar variation characteristics, the estimation accuracy and performance of all models are better than that of B6 battery as the testing set when B5 battery is the testing set, among which the model proposed in this paper is optimal. At this time, the MSE, RMSE, MAE and MAPE corresponding to IB-ELM are 1.46×10^{-4} , 1.21%, 0.97% and 2.8×10^{-3} , respectively.

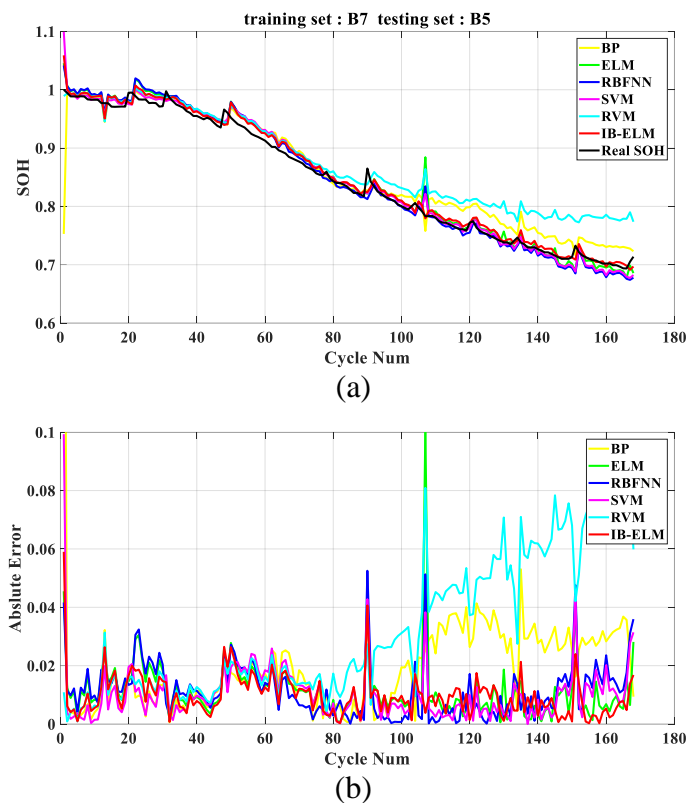


Figure 16. SOH estimation results and absolute error under different models for B5 with training set B7. (a) Estimation results. (b) Absolute Error.

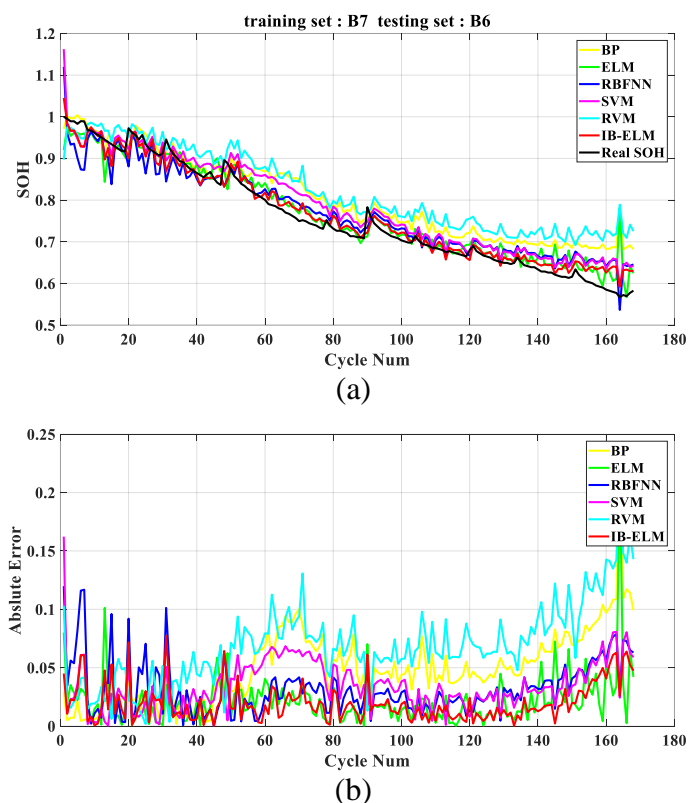


Figure 17. SOH estimation results and absolute error under different models for B6 with training set B7. (a) Estimation results. (b) Absolute Error.

In summary, the model proposed in this paper can provide more stable and accurate estimation results under the interference of non-Gaussian noise. It not only greatly improves the estimation performance and accuracy of traditional ELM, but also improves the adaptability of the model to the environment. Compared to the existing DD methods, this method can not only estimate the SOH of the whole life cycle of LIBs, but also estimate the SOH of different batteries of the same type. In addition, through experiments, we have found that the estimation accuracy of the model is not only disturbed by non-Gaussian noise, but also affected by the training and testing set. Datasets with closer variation characteristics can achieve more accurate estimation.

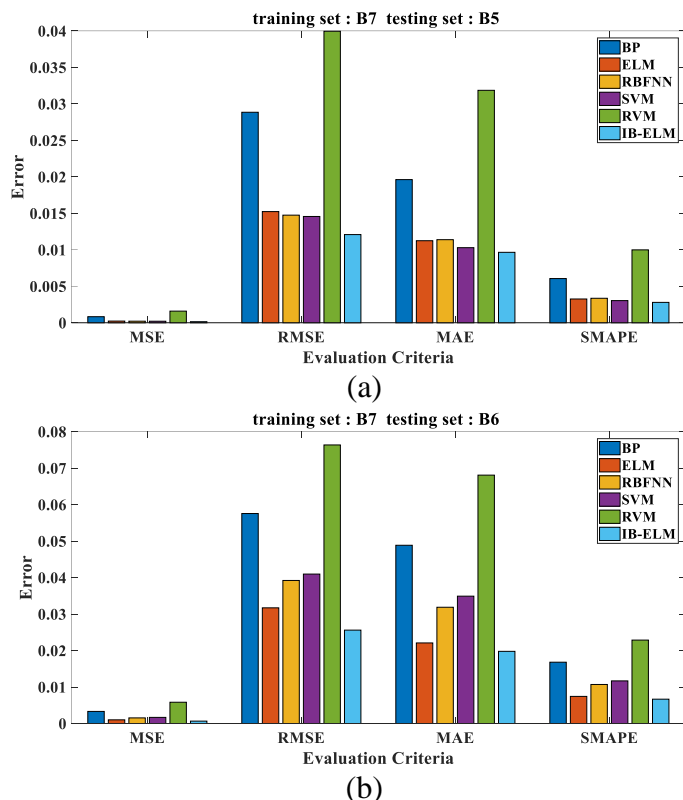


Figure 18. Results of performance evaluation criteria for different models with different testing sets. (a)B5. (b)B6.

Case 4 SOH estimation under different input variate

Generally, for the aging data of LIBs, the charging voltage, current and temperature curves of each cycle are used to extract the HFs as the input vector of SOH estimation. Therefore, appropriate HFs are important factors to realize SOH estimation. The correlation between the selected HFs and SOH has been studied by GRA in section 3.2.4, and we will improve the existing experiment to evaluate the impact of different HFs on SOH estimation by combining different HFs to form new inputs to the model. From **Case 1**, we know that when B5 battery or B7 battery is used as training set and testing set, more accurate SOH estimation can be achieved. Hence, we select B5 battery and B7 battery as the training set and testing set of the model in this experiment.

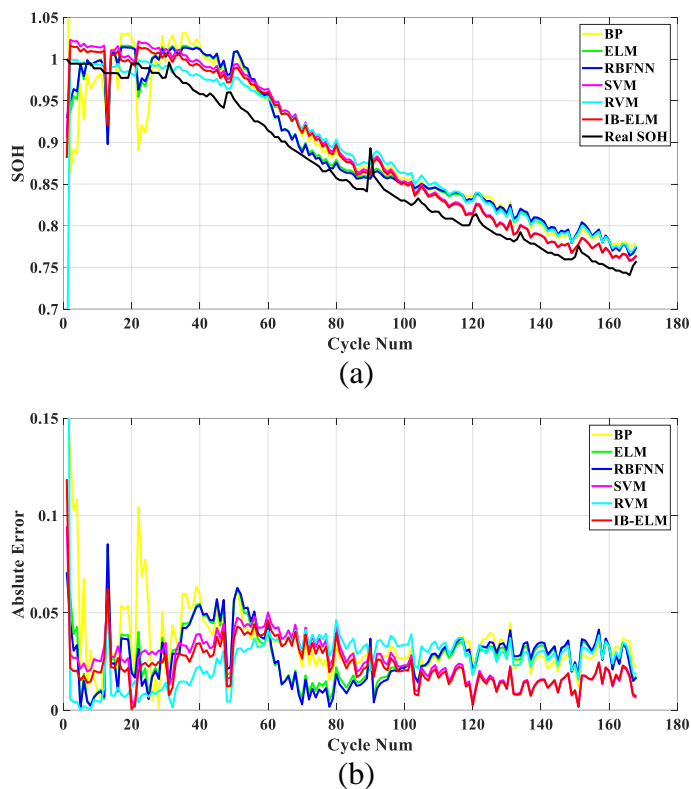


Figure 19. SOH estimation results and absolute error using F_3 as input vector under different models. (a) Estimation results. (b) Absolute Error.

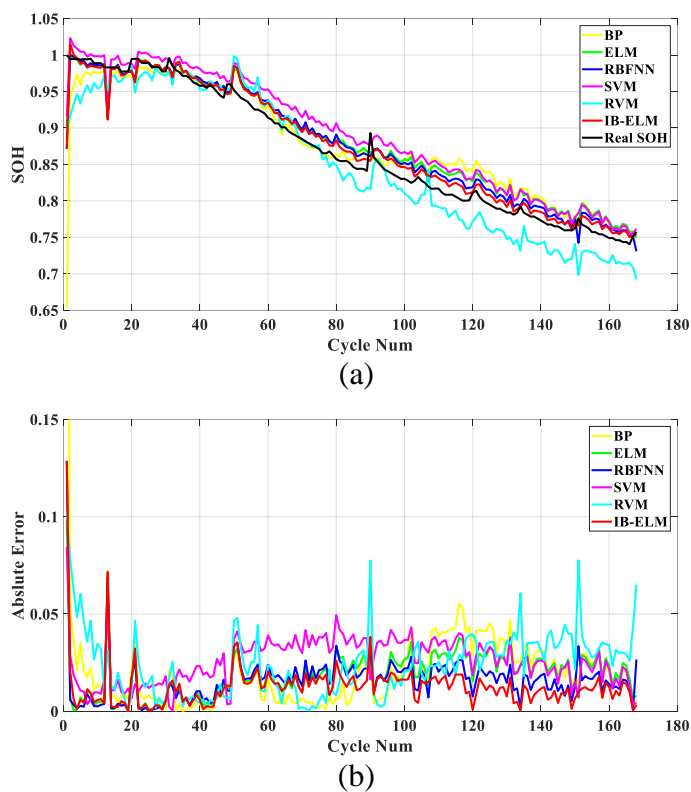


Figure 20. SOH estimation results and absolute error using F_1 - F_3 as input vector under different models. (a) Estimation results. (b) Absolute Error.

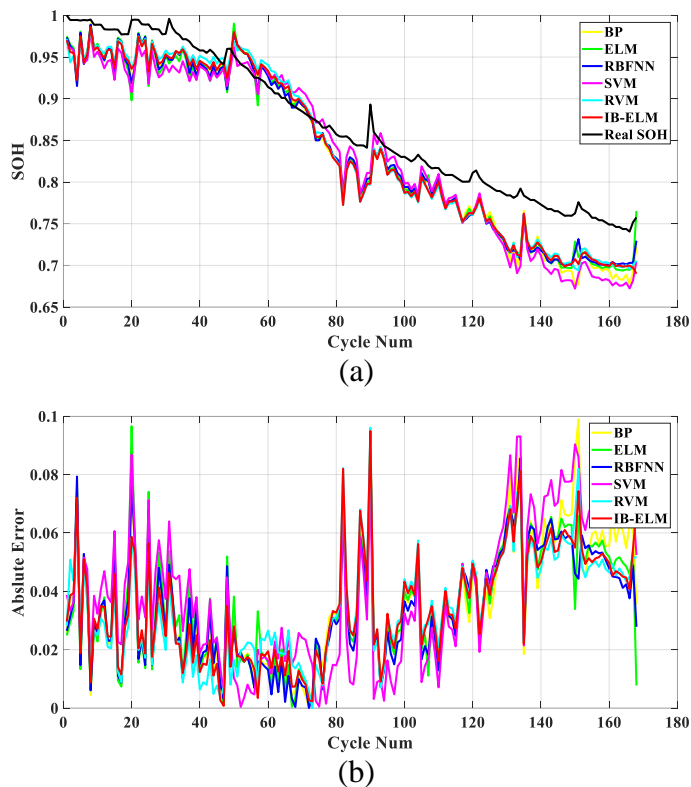


Figure 21. SOH estimation results and absolute error using F_1 - F_2 as input vector under different models. (a) Estimation results. (b) Absolute Error.

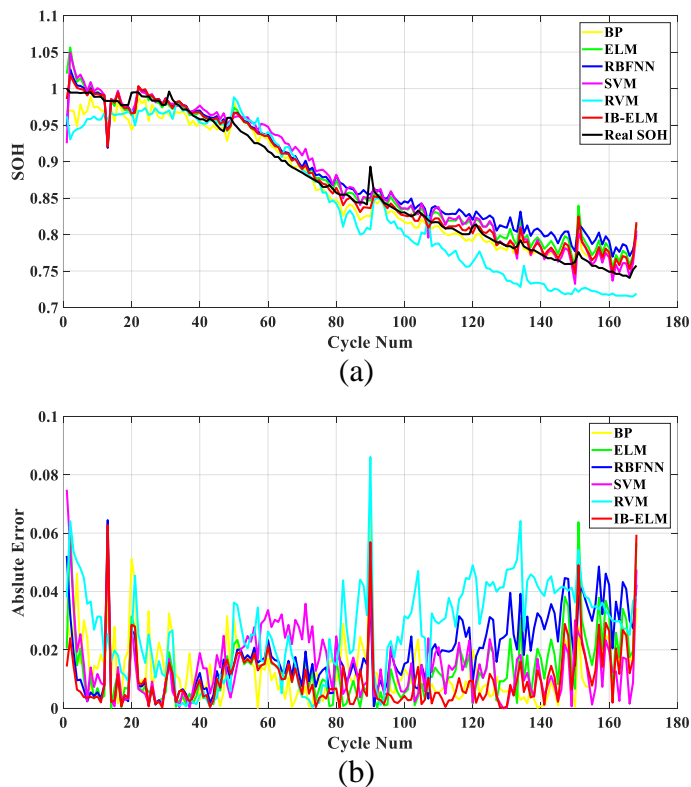


Figure 22. SOH estimation results and absolute error using F_1 - F_2 - F_3 as input vector under different models. (a) Estimation results. (b) Absolute Error.

Relevant parameters settings are the same as **Case 1**. Fig.19-22 show the SOH estimation results and absolute error curves under different combinations of HFs (including F_3 , F_1 - F_3 , F_1 - F_2 , F_1 - F_2 - F_3), and Table 5 shows the performance results of different models under all evaluation criteria.

Table 5. Results of performance evaluation criteria under different input variable.

Input vector	Method	MSE	RMSE	MAE	SMAPE
F_3	BP [45]	1.62E-03	0.0402	0.0346	0.0097
	ELM [38]	9.59E-04	0.0310	0.0278	0.0079
	RBFNN [29]	9.57E-04	0.0309	0.0274	0.0078
	SVM [26]	7.95E-04	0.0282	0.0254	0.0071
	RVM [30]	1.81E-03	0.0426	0.0279	0.0082
	IB-ELM	6.76E-04	0.0260	0.0228	0.0064
F_1 - F_2	BP [45]	1.69E-03	0.0411	0.0354	0.0109
	ELM [38]	1.63E-03	0.0403	0.0351	0.0107
	RBFNN [29]	1.52E-03	0.0389	0.0338	0.0103
	SVM [26]	2.11E-03	0.0459	0.0389	0.0120
	RVM [30]	1.49E-03	0.0386	0.0341	0.0105
	IB-ELM	1.54E-03	0.0393	0.0347	0.0106
F_1 - F_3	BP [45]	1.27E-03	0.0357	0.0209	0.0062
	ELM [38]	4.89E-04	0.0221	0.0185	0.0055
	RBFNN [29]	4.07E-04	0.0202	0.0158	0.0046
	SVM [26]	8.05E-04	0.0284	0.0258	0.0074
	RVM [30]	8.78E-04	0.0296	0.0243	0.0073
	IB-ELM	3.06E-04	0.0175	0.0126	0.0036
F_1 - F_2 - F_3	BP [45]	2.74E-04	0.0165	0.0129	0.0037
	ELM [38]	3.16E-04	0.0178	0.0134	0.0039
	RBFNN [29]	4.88E-04	0.0221	0.0183	0.0055
	SVM [26]	3.44E-04	0.0185	0.0145	0.0042
	RVM [30]	9.78E-04	0.0313	0.0271	0.0082
	IB-ELM	2.03E-04	0.0142	0.0100	0.0029

As can be seen from Fig.19, the estimation results of all models have large deviations when F_3 is used as the only input of the model. In this case, although the estimation effect of IB-ELM model is not satisfactory, the estimation trend can still be consistent with the real SOH because of the strongest correlation between F_3 and SOH. Compared to the single-input model, all models show better estimation results when F_1 and F_3 are the input of the model. As shown in Fig.20, the estimation accuracy of all models is improved. However, for the combination of F_1 and F_2 , all models do not have good estimation performance due to the weak correlation between F_1 , F_2 and SOH, as shown in Fig.21. Finally, according to the results in Fig.22, when all the HFs are selected as the input of the model, each model plays a good estimation effect, which indicates that the HFs F_1 , F_2 , and F_3 as a good input combination could be used to estimate SOH. In addition, although the correlation between some HFs and SOH is low, an appropriate number of HFs can not only improve the estimation accuracy of the model, but also provide more references for SOH estimation, so it can also be considered in SOH estimation. What is more, we can see from Table 5 that when the HFs F_1 , F_2 and F_3 are used as the inputs of the model, the estimation accuracy and stability of IB-ELM studied in this paper are significantly improved under the interference of non-Gaussian noise. The MSE, RMSE, MAE and MAPE are 2.03×10^{-4} , 1.42%, 1.00% and

2.9×10^{-3} , respectively. Consequently, one can conclude that different input vectors also will have different influence on the estimation results of the proposed model.

Case 5 SOH estimation under different free parameters

In Section 2.2, we discussed and studied the IB-Loss function in detail whose performance is affected by different free parameters. Hence, we conduct new experiments using different free parameters (a, b, γ) to assess the performance of IB-ELM in this situation. Similarly, we take B5 battery as the training set, B7 battery as the testing set, and add non-Gaussian noise to the SOH in the training set. Fig.23-25 show the SOH estimation results and absolute error curves of the IB-ELM model with different free parameters (a, b, γ). Table 6 presents the performance results of the proposed model with different free parameters under all evaluation criteria. It can be seen from Fig.23-25 that when two free parameters are determined, the remaining one has a certain impact on the performance of the model. Among them, when γ is used as the uncertain free parameter, the impact on the performance of the model is the greatest. Smaller γ values help enhance the performance of the model.

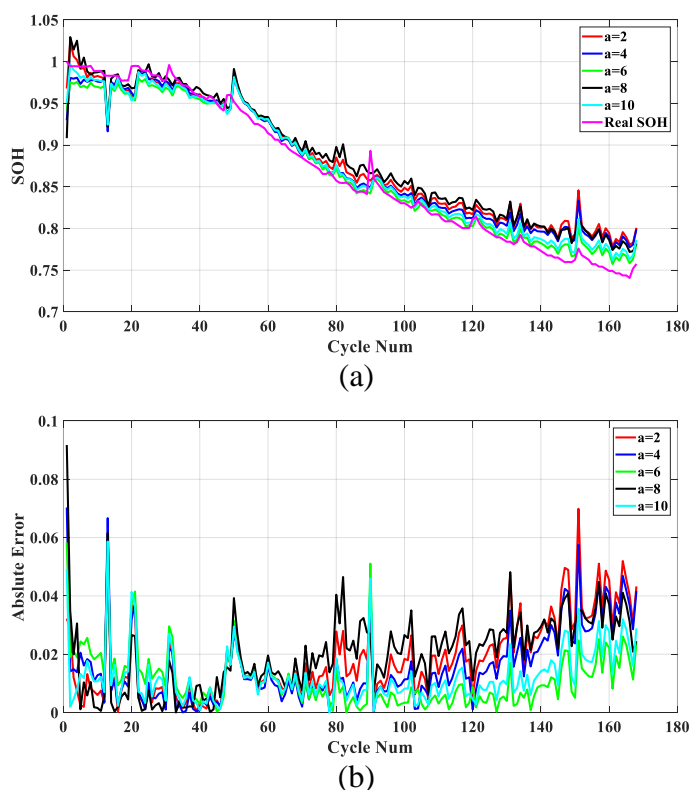


Figure 23. SOH estimation results and absolute error of IB-ELM with different a values ($b = 5, \gamma = 1$). (a) Estimation results. (b) Absolute Error.

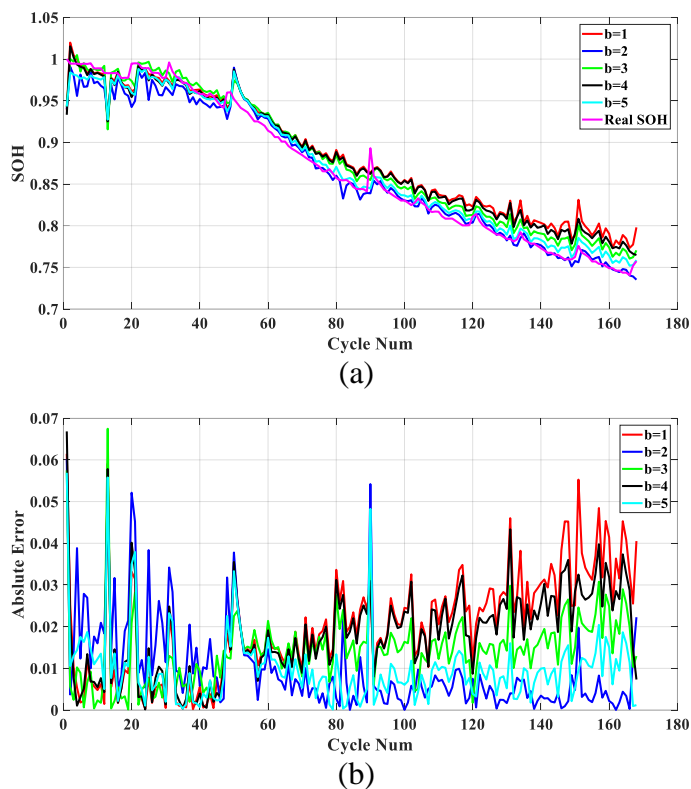


Figure 24. SOH estimation results and absolute error of IB-ELM with different b values ($a = 10, \gamma = 1$). (a) Estimation results. (b) Absolute Error.

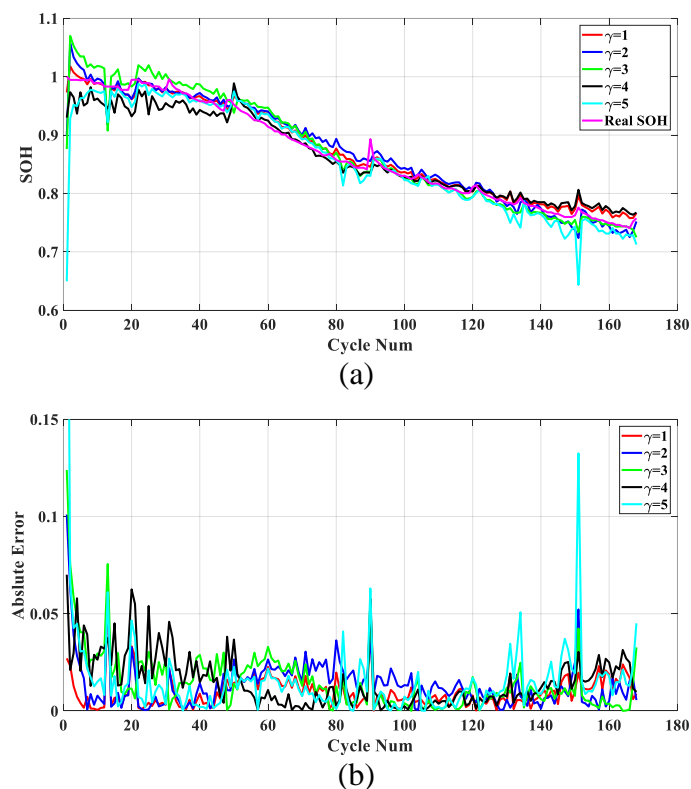


Figure 25. SOH estimation results and absolute error of IB-ELM with different γ values ($a = 5, b = 8$). (a) Estimation results. (b) Absolute Error.

Table 6. Results of performance evaluation criteria with different free parameters.

free parameters	values	MSE	RMSE	MAE	SMAPE
<i>a</i>	2	5.26E-04	0.0229	0.0186	0.0056
	4	4.13E-04	0.0203	0.0157	0.0047
	6	2.18E-04	0.0148	0.0113	0.0032
	8	5.86E-04	0.0242	0.0202	0.0060
	10	2.40E-04	0.0155	0.0124	0.0036
<i>b</i>	1	5.80E-04	0.0241	0.0204	0.0061
	2	2.19E-04	0.0148	0.0099	0.0027
	3	2.80E-04	0.0167	0.0142	0.0042
	4	4.53E-04	0.0213	0.0183	0.0054
	5	1.72E-04	0.0131	0.0099	0.0028
<i>γ</i>	2	1.61E-04	0.0127	0.0097	0.0028
	4	3.36E-04	0.0183	0.0134	0.0038
	6	4.64E-04	0.0215	0.0149	0.0041
	8	4.22E-04	0.0205	0.0153	0.0043
	10	1.20E-03	0.0342	0.0164	0.0049

5. CONCLUSION

The traditional ELM takes MSE as the error criterion with fast learning speed and high generalization ability, and has the best performance in Gaussian noise, which can be used for SOH estimation. However, since EVs usually operate in complex environments, they are easily affected by non-Gaussian noise or other random fluctuations, resulting in greatly reduced stability and generalization ability of the model. Therefore, the traditional ELM may perform unsuitable SOH estimation in presence of non-Gaussian noise environments. To address the problem of inaccurate and unstable estimation model under non-Gaussian noise, an ELM model based on IB-LOSS is studied to realize robust SOH estimation. As a result, the specific work of this paper is as follows: First, we define a new criterion, called IB-LOSS. Secondly, by replacing MSE with IB-LOSS, a new robust ELM model, namely IB-ELM, is derived, which can enhance the stability and estimation accuracy of the traditional ELM model. Third, we use the proposed IB-ELM model for SOH estimation and achieve good estimation results under the condition that the measured data (especially the SOH values as labels) contain non-Gaussian (or outliers) noise. Finally, we evaluate the performance of the proposed model under different experimental conditions, and the experiment results show that the model proposed in this paper can achieve higher estimation accuracy contrast with other existing methods. Moreover, considering the actual working environment of LIBs, the model has a great application prospect.

The SOH estimation in this paper is realized around a single battery. In order to make the model applied in practice situations, it will be our next step to realize the SOH estimation of battery packs in complex environments. In addition, this paper only considers the SOH estimation under a single temperature change (24°C), so studying the SOH estimation under different temperature changes and different charging and discharging modes will also be our research direction. In the future, how to optimize the free parameters in IB-ELM according to different problems will be another focus worthy of research.

ACKNOWLEDGMENT

The work was supported by the National Key R.D Program of China (Grant No. 2021YFB2401904), National Natural Science Foundation of China (Grant No.61976175, 51877174), the Key Laboratory Project of Shaanxi Provincial Education Department Scientific Research Projects (Grant No.20JS109), and Guangxi Key Laboratory of Wireless Wideband Communication and Signal Processing.

References

1. W. He, N. Williard, M. Osterman, M. Pecht, *J. Power Sources*, 196 (2011) 10314.
2. K. A. Severson, P. M. Attia, N. Jin, N. Perkins, B. Jiang, Z. Yang, M. H. Chen, M. Aykol, P. K. Herring, D. Fraggedakis, M. Z. Bazan, S. J. Harris, W. C. Chueh, R. D. Braatz, *Nat. Energy*, 4 (2019) 383.
3. Y. Y. Li, S. M. Zhong, Q. S. Zhong, K. B. Shi, *IEEE Access*, 7 (2019) 8754.
4. D. Wang, Q. Miao, M. Pecht, *J. Power Sources*, 239 (2013) 253.
5. K. Laadjal, A. J. M. Cardoso, *Int. J. Energy Res.*, 45 (2021) 18424.
6. Z. Y. Wu, L. K. Yin, R. Xiong, S. L. Wang, W. Xiao, Y. Liu, J. Jia, Y. C. Liu, *Int. J. Electrochem. Sci.*, 17 (2022) 220754.
7. C. H. Weng, J. Sun, H. Peng, *J. Power Sources*, 258 (2014) 228.
8. L. Chen, W. L. Lin, J. Z. Li, B. B. Tian, H. H. Pan, *Energy*, 106 (2016) 662.
9. K. S. Ng, C. S. Moo, Y. P. Chen, Y. C. Hsieh, *Appl. Energy*, 86(2009)1506.
10. S. Phul, A. Deshpande, B. Krishnamurthy, *Electrochim. Acta*, 164 (2015) 281.
11. Z. L. Wang, G. J. Feng, D. Zhen, F. S. Gu, A. Ball, *Energy Rep.*, 7 (2021) 5141.
12. D. Andre, C. Appel, T. Soczka-Guth, D. U. Sauer, *J. Power Sources*, 224 (2013) 20.
13. S. L. Wang, D. I. Stroe, C. Fernandez, C. M. Yu, C. Y. Zou, X. X. Li, *J. Power Sources*, 450 (2020) 227652.
14. J. Kim, B. H. Cho, *IEEE Trans. Veh. Technol.*, 60 (2011) 4249.
15. R. Xiong, S. L. Wang, C. Fernandez, C. M. Yu, Y. C. Fan, W. Cao, C. Jiang, *Int. J. Electrochem. Sci.*, 16 (2021) 211114.
16. F. Naseri, E. Farjah, T. Ghanbari, Z. Kazemi, E. Schaltz, J. L. Schanen, *IEEE Trans. Ind. Electron.*, 67 (2020) 7963.
17. J. Bi, T. Zhang, H. Y. Yu, Y. Q. Kang, *Appl. Energy*, 182 (2016) 558.
18. J. W. Wei, G. Z. Dong, Z. H. Chen, *IEEE Trans. Ind. Electron.*, 65 (2018) 5634.
19. G. Z. Dong, Z. H. Chen, J. W. Wei, Q. Ling, *IEEE Trans. Ind. Electron.*, 65 (2018) 8646.
20. C. Lyu, Q. Z. Lai, T. F. Ge, H. H. Yu, L. X. Wang, N. Ma, *Energy*, 120 (2017) 975.
21. C. Chen, R. Xiong, W. X. Shen, *IEEE Trans. Power Electron.*, 33 (2018) 332.
22. I. S. Kim, *IEEE Trans. Power Electron.*, 25 (2010) 1013.
23. J. W. Wei, G. Z. Dong, Z. H. Chen, *J. Power Sources*, 397 (2018) 352.
24. X. S. Hu, S. B. Li, H. Peng, *J. Power Sources*, 198 (2012) 359.
25. J. B. Yu, *Reliab. Eng. Syst. Saf.*, 174 (2018) 82.
26. W. Xiong, Y. M. Mo, C. Yan, *IEEE Access*, 9 (2021) 1870.
27. Q. L. Li, D. Z. Li, K. Zhao, L. C. Wang, K. Wang, *J. Energy Storage*, 50 (2022) 104215.
28. Y. Li, C. F. Zou, M. Bercibar, E. Nanini-Maury, J. C. W. Chan, P. V. D. Bossche, J. V. Mierlo, N. Omar, *Appl. Energy*, 232 (2018) 197.
29. C. Q. She, Z. P. Wang, F. C. Sun, P. Liu, L. Zhang, *IEEE Trans. Ind. Inf.*, 16 (2020) 3345.
30. Z. W. Chen, N. Shi, Y. F. Ji, M. Niu, Y. R. Wang, *Energy*, 234 (2021) 121269.
31. Y. T. Zhou, Y. N. Wang, K. Wang, L. Kang, F. Peng, L. C. Wang, J. B. Pang, *Appl. Energy*, 260 (2020) 114169.
32. G. B. Huang, Q. Y. Zhu, C. K. Siew, *Neurocomputing*, 70 (2006) 489.
33. H. P. Wang, X. L. Chu, P. Chen, J. Y. Li, D. Liu, Y. P. Xu, *Fuel*, 309 (2022) 122224.

34. Y. Zhou, N. R. Zhou, L. H. Gong, M. L. Jiang, *Energy*, 204 (2020) 117894.
35. B. Gou, Y. Xu, X. Feng, *IEEE Trans. Transp. Electrification*, 7 (2021) 422.
36. L. Chen, H. M. Wang, B. H. Liu, Y. J. Wang, Y. H. Ding, H. H. Pan, *Energy*, 215 (2021) 119078.
37. D. Z. Li, S. Li, S. B. Zhang, J. R. Sun, L. C. Wang, K. Wang, *Energy*, 250 (2022) 123773.
38. Y. M. Fu, J. Xu, M. J. Shi, X. S. Mei, *IEEE Trans. Ind. Electron.*, 69 (2022) 7019.
39. J. J. Tang, J. H. Li, W. Q. Xu, Y. J. Tian, X. C. Ju, J. Zhang, *Neural Networks*, 143 (2021) 327.
40. B. Frenay, M. Verleysen, *IEEE Trans. Neural Networks Learn. Syst.*, 25 (2014) 845.
41. L. Ungurean, G. Carstoiu, M. V. Micea, V. Groza, *Int. J. Energy Res.*, 41 (2017) 151.
42. B. Saha, K. Goebel, Battery Data Set, Moffett Field, CA, USA: NASA Ames Res. Center, 2007.
[Online]. Available: <https://ti.arc.nasa.gov/tech/dash/groups/pcoe/prognostic-data-repository/>
43. X. S. Hu, Y. H. Che, X. K. Lin, S. Onori, *IEEE Trans. Transp. Electrification*, 7 (2021) 382.
44. N. Tosun, *Int. J. Adv. Manuf. Technol.*, 28 (2006) 450.
45. J. P. Wen, X. Chen, X. H. Li, Y. K. Li, *Energy*, 261 (2022) 125234.

© 2022 The Authors. Published by ESG (www.electrochemsci.org). This article is an open access article distributed under the terms and conditions of the Creative Commons Attribution license (<http://creativecommons.org/licenses/by/4.0/>).